Pax6 loss alters the morphological and electrophysiological development of mouse prethalamic neurons

Tian Tian[1,*], Idoia Quintana-Urzainqui[2], Zrinko Kozić[1], Thomas Pratt[1], David J. Price[1]

[1]Simons Initiative for the Developing Brain, Hugh Robson Building, George Square, Edinburgh EH8 9XD, UK
[2]Developmental Biology Unit, European Molecular Biology Laboratory (EMBL), Meyerhofstrasse 1, 69012 Heidelberg, Germany

* Author for correspondence: ttian@ed.ac.uk

KEYWORDS: Pax6, transcription factors, prethalamus, neuronal morphogenesis, axon initial segment, neuronal activity

SUMMARY STATEMENT

Pax6 impacts neurite extension, axon initial segment properties and ability to fire normal action potentials in maturing neurons, revealing actions extending beyond those previously characterized in progenitors.

ABSTRACT

Pax6 is a well-known regulator of early neuroepithelial progenitor development. Its constitutive loss has a particularly strong effect on the developing prethalamus, causing it to become extremely hypoplastic. To overcome this difficulty in studying the long-term consequences of Pax6 loss for prethalamic development, we used

conditional mutagenesis to delete Pax6 at the onset of neurogenesis and studied the developmental potential of the mutant prethalamic neurons in vitro. We found that Pax6 loss affected their rates of neurite elongation, the location and length of their axon initial segments and their electrophysiological properties. Our results broaden our understanding of the long-term consequences of Pax6 deletion in the developing mouse forebrain, suggesting that it can have cell autonomous effects on the structural and functional development of some neurons.

INTRODUCTION

The early neuroepithelium is patterned by the regional expression of transcription factors that specify the subsequent development of each region. The extent to which the actions of these transcription factors influence the later development of the functional properties of neurons is much less clear.

We studied the transcription factor Pax6, a well-known regulator of early neural development (Cvekl and Callaerts, 2017). Pax6 expression in the mouse neuroepithelium is first detected soon after neural tube closure and continues in specific forebrain progenitors, where it has pivotal functions in diverse early developmental processes (Hanson and Van Heyningen, 1995; Engelkamp *et al.*, 1999; Mi *et al.*, 2013; Manuel *et al.*, 2015; Cvekl and Callaerts, 2017). In most of these regions, Pax6's expression is lost in cells exiting the cell cycle during neurogenesis (Duan *et al.*, 2013). Most, if not all, prethalamic progenitors are Pax6-positive but, unusually, strong Pax6 expression is retained by many post-mitotic neurons in the embryonic prethalamus (Duan *et al.*, 2013; Caballero *et al.*, 2014). Constitutive deletion of Pax6 all but prevents the formation of the prethalamus, precluding an analysis of the consequences of its loss for developing prethalamic neurons (Stoykova *et al.*, 1996; Warren and Price, 1997).

We re-examined our previously-reported RNAseq dataset of changes in prethalamic gene expression following acute Pax6 deletion at the onset of neurogenesis (Quintana-Urzainqui *et al.*, 2018) and found upregulated expression of genes involved in neuronal morphogenesis and ion transport. We investigated the effects of

acute Pax6 deletion on the ability of prethalamic neurons to acquire normal structural and functional properties. We used dissociated culture, thereby increasing the likelihood of detecting cell autonomous effects. We found that the neurites of Pax6-deleted prethalamic neurons grew at abnormal speed, their axon initial segments (AISs) tended to be longer and to extend further from the soma and their electrophysiological properties were altered. Our results indicate that in addition to its role in early prethalamic progenitors, Pax6 is also required in the later structural and functional development of prethalamic neurons.

RESULTS AND DISCUSSION

Prethalamic Pax6 deletion caused upregulation of genes involved in neuronal morphogenesis and ion transport

At E13.5, Pax6 is expressed in cortical, thalamic and prethalamic progenitors and in a population of prethalamic neurons (Supplementary Figure 1A-A'). We interrogated an existing RNAseq dataset showing significant transcriptional changes (adjusted $p<0.05$) in E13.5 prethalamus after acute deletion of Pax6 from E11.5, which is after prethalamic neuroepithelial specification and around the time prethalamic neurogenesis starts (Quintana-Urzainqui *et al.*, 2018). Gene ontology (GO) term enrichment analysis on these genes revealed 495 upregulated and 125 downregulated GO terms (Supplementary Table 1). Among the top 200 upregulated GO terms, 25 related to neuronal morphogenesis and 12 to ion transport. After removing child terms, 14 GO terms were related to neuronal morphogenesis and 7 were related to ion transport (Figure 1A-B, Supplementary Table1).

Pax6 loss upregulated genes important for the actin and microtubule cytoskeleton during neuritogenesis, for axon specification and for neurite elongation (Supplementary Table 2). In other systems, upregulation of these effector genes increases actin nucleation, actin bundling, microtubule assembly and bidirectional intracellular transportation, which have been shown to augment axon/neurite elongation (Witte and Bradke, 2008; Stiess and Bradke, 2011; Flynn, 2013; Sainath and Gallo, 2015). Pax6 loss also upregulated genes involved in relaying extracellular signals to the actin and microtubule cytoskeleton and genes encoding several

components of the PAR3/6 complex, which plays a vital role during the establishment of neuronal polarity (Supplementary Table 2) (Nishimura *et al.*, 2004; Shi *et al.*, 2004; Barnes and Polleux, 2009; Lalli, 2014).

The AIS is located at the axon's most proximal end and is where action potentials usually initiate (Kole and Stuart, 2008; Kole *et al.*, 2008; Rasband, 2010; Leterrier, 2018). Genes encoding the cytoskeletal components of the AIS were also upregulated (Supplementary Table 2), including the cytoskeletal scaffold protein AnkyrinG (AnkG, also known as Ank3) and βIV Spectrin (Sptbn4). In neurons, AnkG is restricted to the AIS and nodes of Ranvier, where it tethers high densities of specific types of voltage gated ion channels and anchors itself to the underlying actin cytoskeleton via βIV Spectrin (Rasband, 2010; Leterrier, 2018). Genes encoding voltage gated sodium channels (VGSCs) that show concentrated distributions within the AIS were also upregulated, as were genes that encode various voltage-gated ion channels expressed within the somatodendritic domain (Lai and Jan, 2006; Hu *et al.*, 2009).

Based on this analysis, we hypothesised that conditional Pax6 deletion affects the morphogenesis, AIS formation and the activity of prethalamic neurons. To test these hypotheses, we measured the effects of the same conditional mutation as in the RNAseq study in an *in vitro* culture system.

Pax6 loss caused defects of neurite extension in developing prethalamic neurons

Our protocol for tamoxifen-induced deletion caused Pax6 protein loss from E11.5 onwards in conditional knockouts (Pax6cKOs, CAG^{CreER} $Pax6^{fl/fl}$) (Quintana-Urzainqui *et al.*, 2018). No Pax6 protein was detected at the time of dissociation at E13.5 (Supplementary Figure 1B-B'). Littermates that were heterozygous for the $Pax6^{fl}$ allele were used as controls (Ctrl, CAG^{CreER} $Pax6^{fl/+}$), as they continue to express Pax6 normally (Simpson *et al.*, 2009).

Figure 2A-E shows the process of E13.5 prethalamic dissection for dissociated cell culture. At each day in vitro (DIV), we measured: the number of neurites; the length of the longest neurite; and the total length of neurites (Figure 2F-F'). Most cultured

Ctrl and Pax6cKO prethalamic cells were positive for Tuj1 and neuritogenesis had begun at 1DIV (Figure 2G-G'). Most prethalamic neurons displayed one longest neurite, presumably the developing axon, and several shorter neurites (Figure 2G-L'). Pax6cKO prethalamic neurons had fewer neurites than Ctrl neurons at 1DIV ($p=7.20x10^{-3}$, n=3, the statistical test is always a mixed-effect model, and the unit of n is always cultures from separate litters unless stated otherwise) but not after longer culture (Figure 2M). The longest neurites and the total neurite lengths in Pax6cKO prethalamic neurons were shorter than in Ctrls from 1-3 DIV (Figure 2N-O). However, after 3DIV the longest neurites elongated more rapidly in Pax6cKO than in Ctrl neurons and they became significantly longer at 5DIV ($p=2.17x10^{-5}$, n=3) and 6DIV ($p=1.66x10^{-6}$, n=3; Figure 2N). Thus, Pax6cKO prethalamic neurons developed a relatively normal complement of neurites after a delayed start, the longest of which later outstripped their equivalents in Ctrl neurons. Mechanisms limiting axon elongation might be important because most prethalamic neurons project only short distances (Martinez-Ferre and Martinez, 2012; Willis *et al.*, 2015), unlike neighbouring thalamic neurons, many of which project long thalamocortical axons.

It is unclear what causes delayed neuronal morphogenesis in Pax6cKO prethalamic neurons early in cell culture. Previous studies proposed that the establishment of neuronal polarity can be a speed-limiting step of neuronal morphogenesis in vitro (Bradke and Dotti, 2000; Barnes and Polleux, 2009; Yogev and Shen, 2017). We examined this further, since the RNAseq analysis indicated that Pax6cKO prethalamic cells upregulated expression of genes encoding components of the Par3/6 complex. We used the localised distribution of Par3 as an indicator of neuronal polarity (Nishimura *et al.*, 2004). Our results showed no significant differences in the amount and distribution of Par3 within the neurites and the soma between Ctrl and Pax6cKO prethalamic neurons at 3DIV (Supplementary Figure 2A-N). Further analysis on neurite organisation and branching showed no significant differences between Ctrl and Pax6cKO neurons (Supplementary Figure 2O-P). We concluded that the establishment of neuronal polarity was not affected in *Pax6*-deleted prethalamic neurons.

Pax6 loss altered AIS length and location in developing prethalamic neurons

We investigated AIS formation with immunohistochemistry for AnkG and VGSC in dissociated prethalamic neurons at 7 and 9 DIV. In these experiments we used an antibody that recognizes an epitope in the C-terminal domain of Pax6 (referred to in Fig. 3A-D as Pax6-C), which is produced even in Pax6cKO neurons due to translation from preserved internal initiation sites (see Methods; (Kammandel *et al.*, 1999; Simpson *et al.*, 2009). This confirmed that we were comparing Ctrl and Pax6cKO neurons that expressed the *Pax6* gene (although the latter did not generate full-length functional Pax6 protein: Supplementary Figure 1B, B').

At both 7DIV and 9DIV, most prethalamic neurons of both genotypes developed a single AIS (Figure 3A-D, magenta segments) where the profiles of AnkG and VGSC expression (quantified as illustrated in Figure. 3A'-D') coincided at the proximal end of a neurite (supporting our conclusion that the establishment of neuronal polarity was unaffected in Pax6cKO prethalamic neurons). AISs tended to extend further from the soma in Pax6cKO neurons (7DIV AnkG, $p=2.94x10^{-3}$; n=3; 9DIV VGSC, $p=4.56x10^{-3}$, n=3; Figure. 3E-G). Average AIS lengths measured with VGSC at 7DIV ($p=0.0140$, n=3) and with AnkG at 9DIV were significantly higher in Pax6cKO neurons ($p=0.0263$, n=3, Figure. 3H, I). In no case were densities of staining (i.e. the average fluorescence intensity per unit length of neurite) with either marker different between the two genotypes (Figure. 3J, K). Figure 3L-M summarises the lengthening and distal extension of the AIS in prethalamic neurons after 7 and 9 DIV.

AIS assembly is considered an intrinsic property of neurons, requiring no extracellular or glial-dependent cues (Ogawa and Rasband, 2008). The observed AIS lengthening was in line with the upregulated expression of VGSCs and AnkG in the RNAseq data, but their distal shift was unexpected. As the master regulator of AIS assembly, AnkG specifies AIS formation and VGSC clustering (Zhou *et al.*, 1998; Rasband, 2010), but little is known about the mechanisms that contribute to the enrichment and targeting of AnkG to the proximal axon and specify AIS location (Rasband, 2010; Berger *et al.*, 2018; Leterrier, 2018).

Loss of Pax6 affected the electrophysiological properties of prethalamic neurons

Since the reported changes of the AIS and the expression of voltage-gated ion channels might change neuronal excitability and electrical functions (Grubb and Burrone, 2010; Grubb *et al.*, 2011; Kaphzan *et al.*, 2011; Höfflin *et al.*, 2017; Booker *et al.*, 2020), we performed whole-cell patch-clamp on prethalamic neurons cultured for 7 and 9 DIV.

To induce action potentials (APs), we stimulated the prethalamic neurons with small depolarising current steps from -60mV. Prethalamic neurons of both genotypes at both ages were able to fire APs (Figure 4A-B'). From 7 to 9DIV, resting membrane potentials (RMPs) became significantly more negative in both the Ctrl ($p=4.94x10^{-3}$, n=4) and Pax6cKO prethalamic neurons ($p=9.55x10^{-4}$, n=4), as expected in maturing neurons (Linaro *et al.*, 2019), with no significant differences between genotypes (7DIV, p=0.515, n=4; 9DIV, p=0.944, n=4, Figure 4C). Figure 4D-E showed how membrane potentials changed in response to specific negative (hyperpolarising) and positive (depolarising) current inputs before rheobases were reached. At 7DIV but not at 9DIV, negative current inputs hyperpolarised membrane potentials significantly more in Pax6cKO than in Ctrl neurons ($p=2.00x10^{-4}$, n=4, Figure 4D-E). Although no differences were found at 7DIV (p=0.0549, n=4), rheobase became significantly lower in Pax6 cKOs at 9DIV ($p=7.70x10^{-3}$, n=4, Figure 4F). The AP threshold remained unchanged at both ages (7DIV, p=0.893, n=4; 9DIV, p=0.945, n=4, Figure 4G).

We examined the waveforms of the first APs fired by the Ctrl and the Pax6cKO prethalamic neurons in response to the current stimulus at their rheobases. Figure 4H-I shows the overlayed example traces of the first APs shown in Figure 4A-B'. AP halfwidth was significantly broader in Pax6cKOs at both ages (7DIV, p=0.0125, n=4; 9DIV, p=0.0102, n=4) and AP height was significantly lower in Pax6cKOs at 7DIV ($p=4.78x10^{-3}$, n=4, Figure 4J-K).

Prethalamic neurons from both genotypes were able to fire multiple APs after rheobases were reached but, at 7DIV, Pax6cKO prethalamic neurons showed a significant reduction in maximum AP number (Figure 4L, $p=1.12x10^{-5}$, n=4). The AP firing frequency in the Pax6cKO neurons at 7DIV was 7± 1.4Hz in comparison to 18.6 ± 1.9Hz in the Ctrl neurons. This phenotype was recovered at 9DIV, when Pax6cKO and Ctrl neurons fired comparable maximum numbers of APs (Figure 4M, p=0.897, n=4). At 9DIV, Pax6 loss also caused a leftward shift in the current-frequency response (Figure 4M), indicating that a similar number of APs were generated using a lower amplitude of current stimulus in the Pax6cKO neurons.

Therefore, Pax6 loss can affect the activity of the prethalamic neurons, resulting in changes in their excitability level, the waveforms of somatic APs and their ability to fire APs repetitively.

The distal shift of the AIS in Pax6cKO neurons might have contributed to the widening of the AP waveforms recorded from their soma as these recordings would have been mainly the backpropagated APs generated at the AIS (Kole, Letzkus and Stuart, 2007) and increasing the distance between the AIS and the soma would increase voltage attenuation, resulting in wider and slower APs. The underlying causes for the decrease in rheobase in the Pax6cKO prethalamic neurons are less clear. Changes in AIS length and location could be a factor since previous studies have shown that both increased length and distal relocation of the AIS can promote excitability (Grubb and Burrone, 2010; Buffington and Rasband, 2011; Kaphzan *et al.*, 2011; Höfflin *et al.*, 2017; Jamann, Jordan and Engelhardt, 2018; Goethals and Brette, 2020). Changes of AIS geometry alone are unlikely to provide a full explanation, however, since theoretical modelling suggests that they would produce a modest decrease (a few mV) in threshold potential (Goethals and Brette, 2020), for which we found no evidence. Therefore, it is likely that changes outside the AIS contributed to the decrease in rheobase in Pax6cKO prethalamic neurons. The surprising observation that 7DIV Pax6cKO prethalamic neurons fired significantly fewer APs and entered the state of depolarization block with significantly lower amplitude of current stimulus despite having significantly longer AISs might be explained in two ways. First, there might be AIS defects; second, RNAseq data

suggested upregulation of several voltage-gated potassium channels belonging to the Kv4 family (Kv4.1(KCND1), Kv4.2(KCND2) and Kv4.3(KCND3), Supplementary Table 2), which can efficiently reduce repetitive firing (Fransén and Tigerholm, 2010; Hermanstyne *et al.*, 2017; Kim *et al.*, 2020).

In conclusion, our results suggest that Pax6 loss from the prethalamic neuroepithelium causes the generation of neurons with an abnormal developmental potential. Mutant prethalamic neurons show subtly disrupted axonal extension, abnormal AISs and somatic AP waveforms and excitability, which might impact on prethalamus-thalamus circuit formation and might contribute to defective nervous system development in PAX6-deficient humans (Kikkawa *et al.*, 2019).

MATERIALS AND METHODS

Experimental Model and Subject Details

Mice colony maintenance and transgenic lines

Mouse lines used to generate tamoxifen-induced deletion of Pax6 throughout the embryo were as described in (Quintana-Urzainqui *et al.*, 2018). Pregnant mice were given 10mg of tamoxifen (Sigma) by oral gavage on embryonic day 9.5 (E9.5) to induce Pax6loxP deletion and embryos were collected on E13.5. Embryos heterozygous for the Pax6flox allele ($Pax6^{fl/+}$; $CAGG^{CreER}$) were used as controls (Ctrl) as previous studies have shown no detectable defects in the forebrain of $Pax6^{fl/+}$ embryos (Simpson *et al.*, 2009). Embryos carrying two copies of the floxed Pax6 allele ($Pax6^{fl/fl}$; $CAGG^{CreER}$) were the experimental conditional knock-out (cKO) group.

For staging of embryos, the first day the vaginal plug was detected was considered as embryonic day 0.5 (E0.5).

All animal husbandry was conducted in accordance with the UK Animal (Scientific Procedures) Act 1986 regulations and all procedures were approved by Edinburgh University's Animal Ethics Committee.

Method Details

Dissociated prethalamic cell culture preparation

Dissection of the prethalamus

Dissection of the prethalamus at E13.5 was first practiced extensively using the DTy54 transgene mouse line, as specified previously (Quintana-Urzainqui *et al.*, 2018). Guidance by the GFP expression, which marked Pax6-expressing cells, allowed us to identify reliable morphological landmarks. To dissect the prethalamus, $Pax6^{fl/+}$; $CAGG^{CreER}$ and $Pax6^{fl/fl}$; $CAGG^{CreER}$ embryos from E13.5 were collected and decapitated. The neural tube was separated from the epidermal and mesodermal tissue and cut in half along the dorsal and ventral midline (Figure 2A-B). From E9.5, morphologic segmentation of the diencephalon starts and the diencephalic prosomeres become apparent from E10-11 as ventricular ridges and lateral wall bulges appear (Vieira *et al.*, 2009). These morphological landmarks were used to distinguish prethalamus from the surrounding tissue (the thalamus and the eminentia thalami) during dissection (Figure 2C).

Dissociated cell culture

After being cut out, the prethalamus from the two halves of the neural tube of the same embryo were put together and chopped into smaller pieces for dissociated cell culture using the Papain Dissociation System (Worthington Biochemical Corp.) according to the manufacturer's protocol (Figure 2C-E). The prethalamus from each embryo was dissociated and cultured individually. The number of cells obtained after dissociation was measured using a haemocytometer. Additionally, trypan blue staining was used to determine the ratio of viable to damaged cells. To adjust the plating density of the cell culture, cells obtained after dissociation were resuspended using a certain amount of culture medium (Advanced DMEM/Neurobasal medium 1:1, supplemented with N2 (100x) and B27 (50x) neural supplement, Thermo Fisher Scientific). 130µl of the culture medium containing the desired number of resuspended cells was then added onto the 9mm circular coverslips (Fischer Scientific) coated with Poly-L-lysine and Laminin (Thermo Fisher Scientific). Due to the surface tension of the culture medium, the culture medium containing the dissociated cells would stay within and fill up the realm of the coverslips. The cell

cultures were then incubated at 37°C with 5% CO2 for 1 hour to allow the cells to attach to the coverslips. In this way, all the cells obtained after the dissociation was retained within the coverslip, and the exact cell density of plating could be calculated using the total amount of cells divided by the surface areas of the coverslips being used. The plating density of prethalamic cell culture used for studying neuronal morphogenesis and AIS formation was 20 cells/mm^2, and the plating density of prethalamic cell culture used for electrophysiological recordings was 600 cells/mm^2. After 1hr, 240µl of the culture medium was then added into each well of the 48-well plate (Greiner Bio-One) that contains the coverslip. The dissociated prethalamic cells were cultured for 1-9 days. Light microscopy was used to monitor the condition of cell cultures daily.

Genotyping

We dissected tissue from the tails of each embryo, extracted DNA and performed PCR amplification to detect the alleles of interest.

For the detection of the floxed Pax6 allele, PCR reaction was performed in a final volume of 25µl containing 1.5µl of extracted DNA, 0.5mM primer mix (Simpson et al. 2009, forward primer: 5'-AAA TGG GGG TGA AGT GTG AG-3'; reverse primer: 5'-TGC ATG TTG CCT GAA AGA AG-3'), 0.5 mM dNTPs mix, 1X PCR reaction buffer and 5U/µl Taq DNA Polymerase (Qiagen). PCR was performed with 35 cycles and a Tm of 59°C. The PCR product was subsequently run in a 2% agarose gel. Wild type allele results in a fragment of 156bp and floxed allele fragment was 195bp, therefore two bands indicated the heterozygous condition (used as controls) and one strong 195bp band identified the homozygous floxed allele condition (Pax6cKOs).

Histological processing and imaging

Sample processing for immunohistochemistry

Cryo-sections were obtained following methods described in (Quintana-Urzainqui *et al.*, 2018).

Cell culture samples were obtained by removing the coverslips containing the prethalamic neurons from the culture medium. 1x phosphate buffered saline (PBS) warmed to 37°C were used to rinse the prethalamic neurons for 3 times. For cell culture samples used in neuronal morphology and polarity studies, the prethalamic neurons were fixed in 4% PFA for 20 minutes. For cell culture samples used in AIS study, the prethalamic neurons were fixed in 2% PFA/4% sucrose for 10 minutes to prevent degradation of AnkG protein by the fixative. The cell culture samples were further rinsed with 1x PBS and kept in 1x PBS at 4°C until processed.

Fluorescent immunohistochemistry

Fluorescent immunohistochemistry on cryo-sections were performed as described in (Quintana-Urzainqui *et al.*, 2018).

Fluorescent immunohistochemistry on cell culture were performed as follows: fixed prethalamic neurons were rinsed with 0.1% Triton X-100 in 1xPBS (0.1% PBST) and permeabilised in 0.5% Triton X-100 in 1x PBS (0.5% PBST) for 10 minutes. Then cells were washed with 0.1% PBST for three times and further blocked with blocking solution (20% goat or donkey serum in 0.1% PBST) for 2 hours. Then the blocking serum containing primary antibodies was added to the cells for overnight incubation. On the second day, cells were washed with 0.1% PBST and further incubated with blocking serum containing the corresponding secondary antibodies (Streptavidin Alexa Fluor^{TM} 488, 546 or 647 conjugates; Thermo Fisher Scientific) for 1 hour. Cells were then washed with 1xPBS, and further incubated with DAPI (Thermo Fisher Scientific) for counterstaining of the nucleus. The coverslips were mounted in ProLong Gold Antifade Mountant (Thermo Fisher Scientific) for further imaging.

Mouse monoclonal anti-Pax6 (1:10) was used to detect the N-terminal domain of Pax6 that is absent in the Pax6$^{fl/fl}$; CAGG^{CreER} embryos (Simpson *et al.*, 2009). Rabbit polyclonal anti-Pax6 (1:200) was used to identify dissociated Ctrl and Pax6cKO prethalamic neurons that expressed the *Pax6* gene as this antibody recognizes an epitope in the C-terminal domain of Pax6, which is produced even in Pax6cKO neurons due to translation from preserved internal initiation sites

((Kammandel *et al.*, 1999; Simpson *et al.*, 2009). Antibody details can be found in the Key Resource Table.

Imaging

Fluorescence images of the dissociated cells in the neuronal morphogenesis study were taken using a Leica DM5500B automated upright microscope connected to a DFC360FX camera. The route of acquiring images started from the upper-left corner towards the lower-right of the 9mm circular coverslip. Every image being taken was from an adjacent visual field of the previous image to cover as many cells on the coverslip as possible and without imaging the same cells twice.

Fluorescence images of the dissociated cells in the PAR3 study were taken using the Zeiss LSM800 confocal microscope with Airy Scan.

Fluorescence images of the dissociated cells in the AIS study were taken using the Andor Revolution XDi Spinning disk confocal microscope.

Whole-cell patch-clamp recording

For electrophysiological recordings on the dissociated prethalamic neurons cultured for 7 and 9 DIV, coverslips with attached prethalamic neurons were transferred to a submerged recording chamber perfused with carbonated ACSF (in mM: 150 NaCl, 2.8 KCl, 10 HEPES, 2 CaCl2, 1 MgCl2, 10 Glucose, pH7.3), at a flow rate of 4-6ml/min at 22-23°C. Prethalamic neurons were visualised with a digital camera (SciCam Pro, Scientifica) mounted on an upright microscope (BX61-WI, Olympus) and a 40x water-immersion objective lens (1.0 N.A., Olympus). Whole-cell patch-clamp recordings were performed with a Multiclamp 700B amplifier (Molecular Devices), filtered at 10KHz with the built-in 4-pole Bessel Filter and digitised using a Digidata 1440A digitiser board (Molecular Devices) at 20kHz. Recording pipettes were pulled from borosilicate glass capillaries (Havard Apparatus, 30-0060) on a horizontal electrode puller (P-97, Sutter Instruments) to a tip resistance of 4-6 MΩ. Recording pipettes were filled with K-gluconate-based internal solution (in mM: 130 K-gluconate, 4 Glucose, 10 HEPES, 0.1 EGTA, 0.025 CaCl2, 20 Sucrose, pH=7.2,

290-300mOsm). Recording pipettes were positioned with a micromanipulator (Scientifica PatchStar). Data were acquired from cells with access resistance < 25MΩ. pClamp 10 (Axon Instruments) was used to generate the various analogue waveforms to control the amplifier and record the traces.

Resting membrane potential of the prethalamic neurons was recorded with current clamped with no current input (I=0 pA) for 30 seconds. Constant current was injected to hold the cells close to -60mV and I-V curve, rheobase and threshold was assessed by current injections from -30 to +140 pA for 1000 ms (10 pA steps). All AP properties were determined from the first AP elicited at rheobase. Analysis of electrophysiological data was performed offline using a custom-written Matlab script kindly provided by Dr Adam Jackson, blind to genotype.

Image analysis

Measurement of neurite length

Measurement of neurite length was performed using the freehand line tool in the FIJI package of ImageJ. Whole morphology of the neurons was marked by fluorescent immunohistochemistry reacting with the Tuj1 antibody, which labels the neuron-specific Class III β-tubulin of the cytoskeleton. For each Tuj1-positive cell, three parameters - the number of neurites, the length of the longest neurite and the total length of neurites were measured. A neurite was defined as a stable protrusion from the soma with strong Tuj1 staining. Protrusions from the soma that were thin and had faint Tuj1 staining were considered as either artefacts or filopodia, which mainly consist of F-actin and were not considered as neurites. The length of a neurite was measured by tracing down the neurite from the edge of the soma to the most distal edge of Tuj1 staining. Such measurement was performed for every neurite of each neuron analysed. The length of the longest neurite was the highest reading among these measurements of each neuron. All the protrusions, positive for Tuj1 staining that stemmed from the neurites were considered as branches. The length of each branch was measured from where it stemmed from the neurite to its furthest edge of Tuj1 staining. The total length of neurites for each neuron was calculated as the sum of the length of all the neurites and branches.

Measurement of PAR3 distribution

Measurement was performed with the IMARIS software (Bitplane, version 9.1.2). Dissociated prethalamic neurons cultured for 3DIV were marked by fluorescent immunohistochemistry reacting with antibodies for PAR3, GFP for whole-cell morphology and DAPI for counterstaining of the nucleus.

The surface function of IMARIS was utilised to create a new GFP channel. To do so, the signal intensity threshold was adjusted manually based on the specific situation of each neuron so that IMARIS was able to detect the space where the GFP signal is above that set threshold. This threshold was determined by fitting and adjusting different threshold values so that the GFP-positive space IMARIS detected optimally matched the actual cytoplasmic volume and included almost all the neurites and cytoplasmic protrusions. Places where their GFP signals were above this threshold but resided outside of the cytoplasm were manually deleted. In this way, a new GFP channel was created, which only included and highly resembled the entire cytoplasm of the neurons. Then a new PAR3 channel was created using the new GFP channel as the template of the cytoplasmic volume to exclude any Par3 staining outside of the cytoplasm. With this new PAR3 channel, we could then detect the highest intensity of PAR3 expression within the cytoplasm. Different thresholds were set for IMARIS to detect the cytoplasmic volumes in which the PAR3 intensities were above 75%, 50%, 25% and 10% of its own highest intensity value. This allowed us to quantify the cytoplasmic volume that had higher expression levels of PAR3 at each of these thresholds, and also visualise the distribution of different intensities of PAR3 within the cytoplasm.

Sholl analysis and neurite branching analysis

Sholl analysis was performed as similarly to previously described (Thongkorn *et al.*, 2021), but using the Sholl Analysis Plugin (https://github.com/morphonets/SNT) of ImageJ2 (Version: 2.3.0/1.53f). Whole-cell morphology of dissociated prethalamic neurons cultured for 3DIV were marked by fluorescent immunohistochemistry reacting with antibodies for GFP for whole-cell morphology and DAPI for counterstaining of the nucleus. The images of these neurons were taken with the

Zeiss LSM800 confocal microscope with Airy Scan then converted into 2D images with maximum intensity projection on Z-stack. A threshold was set to include as much as the whole morphology of each neuron. To construct the circles to perform the Sholl analysis, the centre of the soma was marked manually and circles of radii from 0 to 240 μm from the soma was constructed with 10 μm increment.

To count the number of branches per neuron, the surface function of IMARIS was utilised to create a new GFP channel for the whole-cell morphology of each neuron. The number of branches per neuron was counted as branch points plus the number of end branches that were GFP-positive.

Measurement of the intensity profile of AIS

The intensity profile of AIS was generated by tracing down the neurite bearing the localised expression of either AnkG or VGSC, 80μm from the edge of the soma, using the freehand line tool in the FIJI package of ImageJ, resulting in a graph with the level of AnkG or VGSC expression at each pixel from the soma corresponding to the specific distance from the soma.

Quantification and Statistical Analysis

All experiments were performed blind to genotype. All data was analysed with either a linear mixed-effect model (LMM) or its generalised form (GLMM), unless stated otherwise. The variability due to random effects (animal, litter) was taken into account, allowing for the calculation of the genotype effect size. Where reported, statistical significance was assumed if $p<0.05$.

Key Resource Table

Reagent or Resource	Source	Identifier
Antibodies		
Rabbit polyclonal anti-Pax6 (1:200)	BioLegend	Cat#901301, RRID: AB_2565003
Mouse monoclonal anti-Pax6 (1:10)	A gift from Prof. V van Heyningen, AD2.38 Simpson *et al.*, 2009	N/A
Mouse monoclonal anti-Beta III tubulin (Tuj1) (1:200)	Abcam	Cat# ab18207, RRID: AB_444319
Mouse monoclonal anti-Ankyrin-G, clone N106/36 (1:200)	Antibodies Inc.	Cat# 75-146
Monoclonal Anti-Sodium Channel, Pan antibody produced in mouse (1:100)	Sigma-Aldrich	Cat# S8809-.1MG
Rabbit polyclonal Anti-Partitioning-defective 3 Antibody (1:100)	Millipore	Cat# 07-330
Goat polyclonal Anti-GFP antibody (1:200)	Abcam	Cat# ab6673
Chicken polyclonal Anti-GFP antibody (1:200)	Abcam	Cat# ab13970
Goat anti-mouse biotinylated secondary antibody (1:200)	Vector laboratories	Cat# BA-9200, RRID:AB_2336171
Goat anti-rabbit biotinylated secondary antibody (1:200)	Vector laboratories	Cat# BA-1000, RRID:AB_2313606
Donkey anti-mouse Alexa 568 secondary antibody (1:200)	Thermo Fisher Scientific	Cat# A10037, RRID:AB_2534013
Donkey anti-rabbit Alexa 647 secondary antibody (1:200)	Invitrogen	Cat # A-31573
Donkey anti-chicken Alexa 488 secondary antibody (1:200)	Stratech Scientific Limited	Cat# 703-545-155-JIR
Donkey anti-rabbit Alexa 568 secondary antibody (1:200)	Invitrogen	Cat # A10042
Donkey anti-goat Alexa 488 secondary antibody (1:200)	Invitrogen	Cat # A-11055
Donkey anti-rat Alexa 488 secondary antibody (1:200)	Thermo Fisher Scientific	Cat# A-21208, RRID:AB_141709
Streptavidin, Alexa Fluor 488 conjugate antibody (1:200)	Thermo Fisher Scientific	Cat# S11223, RRID:AB_2336881

Chemicals, Peptides, and Recombinant Proteins		
Tamoxifen	Sigma-Aldrich	T5648; CAS: 10540-29-1
Critical Commercial Assays		
DAB peroxidase substrate kit	Vector Laboratories	SK4100
Papain Dissociation System	Worthington Biochemical Corp	Cat# LK003150
Experimental Models: Organisms/Strains		
Mouse: CAGGCre-ERTM; RCE (GFP)	This paper Hayashi and McMahon, 2002 Sousa et al., 2009	N/A
Mouse: Pax6loxP	Simpson et al., 2009	N/A
Software and Algorithms		
Graphpad Prism 8	Graphpad software	
pClamp	Molecular Devices	
Matlab_R2018b	Mathworks	
Fiji (Image J)	Schindelin et al., 2012	https://fiji.sc/
IMARIS 9.1.2	Bitplane	

Acknowledgement

The authors would like to thank Dr Adam Jackson and Dr Javier Moral-Sanz for assistance with experimental set up for whole-cell patch-clamp recordings, Dr Michael Daw and Dr Sam Booker for comments on the manuscript and all of the members of the Developmental Biology User Group for helpful discussion.

Competing Interests

The authors declare no competing interest.

Funding

This work was supported by: MRC (Mr/J003662/1; Mr/N012291/1), BBSRC (Bb/N006542/1) and SIDB.

Author Contributions

T.T., I.Q.-U., T.P., and D.J.P. were involved in overall conceptualization, data interpretation, and manuscript preparation. T.T. carried out wet-laboratory experiments; Z.K. and T.T. did the bioinformatics and statistics. D.J.P. acquired funding and I.Q.-U., T.P. and D.J.P. supervised the work.

Resource Availability

Lead contact

Further information and requests for resources and reagents should be directed to and will be fulfilled by the Lead Contact, ttian@ed.ac.uk

Materials Availability

This study did not generate new unique reagents.

Data and Code Availability

All data and code generated in this study will be made available upon reasonable request.

The published article (Quintana-Urzainqui *et al.*, 2018) includes all the RNAseq dataset analysed during this study.

References

Barnes, A. P. and Polleux, F. (2009) 'Establishment of axon-dendrite polarity in developing neurons', *Annual review of neuroscience*, 32.

Berger, S. L. *et al.* (2018) 'Localized myosin II activity regulates assembly and plasticity of the axon initial segment', *Neuron*. Elsevier, 97(3), pp. 555–570.

Booker, S. A. *et al.* (2020) 'Input-Output Relationship of CA1 Pyramidal Neurons Reveals Intact Homeostatic Mechanisms in a Mouse Model of Fragile X Syndrome', *Cell Reports*. Elsevier, 32(6), p. 107988.

Bradke, F. and Dotti, C. G. (2000) 'Establishment of neuronal polarity: lessons from cultured hippocampal neurons', *Current opinion in neurobiology*. Elsevier, 10(5), pp. 574–581.

Buffington, S. A. and Rasband, M. N. (2011) 'The axon initial segment in nervous system disease and injury', *European Journal of Neuroscience*. Wiley Online Library, 34(10), pp. 1609–1619.
Caballero, I. M. *et al.* (2014) 'Cell-autonomous repression of Shh by transcription factor Pax6 regulates diencephalic patterning by controlling the central diencephalic organizer', *Cell reports*. Elsevier, 8(5), pp. 1405–1418.
Cvekl, A. and Callaerts, P. (2017) 'PAX6: 25th anniversary and more to learn', *Experimental eye research*. Elsevier, 156, pp. 10–21.
Duan, D. *et al.* (2013) 'Spatiotemporal expression patterns of Pax6 in the brain of embryonic, newborn, and adult mice', *Brain Structure and Function*. Springer, 218(2), pp. 353–372.
Engelkamp, D. *et al.* (1999) 'Role of Pax6 in development of the cerebellar system', *Development*. The Company of Biologists Ltd, 126(16), pp. 3585–3596.
Flynn, K. C. (2013) 'The cytoskeleton and neurite initiation', *Bioarchitecture*. Taylor & Francis, 3(4), pp. 86–109.
Fransén, E. and Tigerholm, J. (2010) 'Role of A-type potassium currents in excitability, network synchronicity, and epilepsy', *Hippocampus*. Wiley Online Library, 20(7), pp. 877–887.
Fukata, Y. *et al.* (2002) 'CRMP-2 binds to tubulin heterodimers to promote microtubule assembly', *Nature cell biology*. Nature Publishing Group, 4(8), pp. 583–591.
Goethals, S. and Brette, R. (2020) 'Theoretical relation between axon initial segment geometry and excitability', *Elife*. eLife Sciences Publications Limited, 9, p. e53432.
Grubb, M. S. *et al.* (2011) 'Short-and long-term plasticity at the axon initial segment', *Journal of Neuroscience*. Soc Neuroscience, 31(45), pp. 16049–16055.
Grubb, M. S. and Burrone, J. (2010) 'Activity-dependent relocation of the axon initial segment fine-tunes neuronal excitability', *Nature*. Nature Publishing Group, 465(7301), pp. 1070–1074.
Hanson, I. and Van Heyningen, V. (1995) 'Pax6: more than meets the eye', *Trends in Genetics*. Elsevier, 11(7), pp. 268–272.
Hermanstyne, T. O. *et al.* (2017) 'Acute knockdown of Kv4. 1 regulates repetitive firing rates and clock gene expression in the suprachiasmatic nucleus and daily rhythms in locomotor behavior', *Eneuro*. Society for Neuroscience, 4(3).

Höfflin, F. *et al.* (2017) 'Heterogeneity of the axon initial segment in interneurons and pyramidal cells of rodent visual cortex', *Frontiers in Cellular Neuroscience*. Frontiers, 11, p. 332.
Hu, W. *et al.* (2009) 'Distinct contributions of Na v 1.6 and Na v 1.2 in action potential initiation and backpropagation', *Nature neuroscience*. Nature Publishing Group, 12(8), pp. 996–1002.
Jamann, N., Jordan, M. and Engelhardt, M. (2018) 'Activity-dependent axonal plasticity in sensory systems', *Neuroscience*. Elsevier, 368, pp. 268–282.
Kammandel, B. *et al.* (1999) 'Distinctcis-Essential Modules Direct the Time–Space Pattern of thePax6Gene Activity', *Developmental biology*. Elsevier, 205(1), pp. 79–97.
Kaphzan, H. *et al.* (2011) 'Alterations in intrinsic membrane properties and the axon initial segment in a mouse model of Angelman syndrome', *Journal of Neuroscience*. Soc Neuroscience, 31(48), pp. 17637–17648.
Kikkawa, T. *et al.* (2019) 'The role of Pax6 in brain development and its impact on pathogenesis of autism spectrum disorder', *Brain research*. Elsevier, 1705, pp. 95–103.
Kim, K.-R. *et al.* (2020) 'Kv4. 1, a key ion channel for low frequency firing of dentate granule cells, is crucial for pattern separation', *Journal of Neuroscience*. Soc Neuroscience, 40(11), pp. 2200–2214.
Kole, M. H. P. *et al.* (2008) 'Action potential generation requires a high sodium channel density in the axon initial segment', *Nature neuroscience*. Nature Publishing Group, 11(2), pp. 178–186.
Kole, M. H. P., Letzkus, J. J. and Stuart, G. J. (2007) 'Axon initial segment Kv1 channels control axonal action potential waveform and synaptic efficacy', *Neuron*. Elsevier, 55(4), pp. 633–647.
Kole, M. H. P. and Stuart, G. J. (2008) 'Is action potential threshold lowest in the axon?', *Nature neuroscience*. Nature Publishing Group, 11(11), pp. 1253–1255.
Lai, H. C. and Jan, L. Y. (2006) 'The distribution and targeting of neuronal voltage-gated ion channels', *Nature Reviews Neuroscience*. Nature Publishing Group, 7(7), pp. 548–562.

Lalli, G. (2014) 'Regulation of neuronal polarity', *Experimental cell research*. Elsevier, 328(2), pp. 267–275.
Leterrier, C. (2018) 'The axon initial segment: an updated viewpoint', *Journal of Neuroscience*. Soc Neuroscience, 38(9), pp. 2135–2145.
Linaro, D. *et al.* (2019) 'Xenotransplanted human cortical neurons reveal species-specific development and functional integration into mouse visual circuits', *Neuron*. Elsevier, 104(5), pp. 972–986.
Manuel, M. N. *et al.* (2015) 'Regulation of cerebral cortical neurogenesis by the Pax6 transcription factor', *Frontiers in cellular neuroscience*. Frontiers, 9, p. 70.
Martinez-Ferre, A. and Martinez, S. (2012) 'Molecular regionalization of the diencephalon', *Frontiers in neuroscience*. Frontiers, 6, p. 73.
Mi, D. *et al.* (2013) 'Pax6 exerts regional control of cortical progenitor proliferation via direct repression of Cdk6 and hypophosphorylation of pRb', *Neuron*. Elsevier, 78(2), pp. 269–284.
Nishimura, T. *et al.* (2004) 'Role of the PAR-3–KIF3 complex in the establishment of neuronal polarity', *Nature cell biology*. Nature Publishing Group, 6(4), pp. 328–334.
Norris, A. D., Dyer, J. O. and Lundquist, E. A. (2009) 'The Arp2/3 complex, UNC-115/abLIM, and UNC-34/Enabled regulate axon guidance and growth cone filopodia formation in Caenorhabditis elegans', *Neural development*. Springer, 4(1), p. 38.
Ogawa, Y. and Rasband, M. N. (2008) 'The functional organization and assembly of the axon initial segment', *Current opinion in neurobiology*. Elsevier, 18(3), pp. 307–313.
Quintana-Urzainqui, I. *et al.* (2018) 'Tissue-Specific Actions of Pax6 on Proliferation and Differentiation Balance in Developing Forebrain Are Foxg1 Dependent', *Iscience*. Elsevier, 10, pp. 171–191.
Rasband, M. N. (2010) 'The axon initial segment and the maintenance of neuronal polarity', *Nature Reviews Neuroscience*. Nature Publishing Group, 11(8), pp. 552–562.
Reinhard, M., Jarchau, T. and Walter, U. (2001) 'Actin-based motility: stop and go with Ena/VASP proteins', *Trends in biochemical sciences*. Elsevier, 26(4), pp. 243–249.
Sainath, R. and Gallo, G. (2015) 'Cytoskeletal and signaling mechanisms of neurite formation', *Cell and tissue research*. Springer, 359(1), pp. 267–278.

Shi, S.-H. *et al.* (2004) 'APC and GSK-3β are involved in mPar3 targeting to the nascent axon and establishment of neuronal polarity', *Current Biology*. Elsevier, 14(22), pp. 2025–2032.
Da Silva, J. S. and Dotti, C. G. (2002) 'Breaking the neuronal sphere: regulation of the actin cytoskeleton in neuritogenesis', *Nature Reviews Neuroscience*. Nature Publishing Group, 3(9), pp. 694–704.
Simpson, T. I. *et al.* (2009) 'Normal ventral telencephalic expression of Pax6 is required for normal development of thalamocortical axons in embryonic mice', *Neural development*. Springer, 4(1), p. 19.
Stiess, M. and Bradke, F. (2011) 'Neuronal polarization: the cytoskeleton leads the way', *Developmental neurobiology*. Wiley Online Library, 71(6), pp. 430–444.
Stoykova, A. *et al.* (1996) 'Forebrain patterning defects in Small eye mutant mice', *Development*. The Company of Biologists Ltd, 122(11), pp. 3453–3465.
Thongkorn, S. *et al.* (2021) 'Sex differences in the effects of prenatal bisphenol A exposure on autism-related genes and their relationships with the hippocampus functions', *Scientific reports*. Nature Publishing Group, 11(1), pp. 1–19.
Vieira, C. *et al.* (2009) 'Molecular mechanisms controlling brain development: an overview of neuroepithelial secondary organizers', *International Journal of Developmental Biology*. UPV/EHU Press, 54(1), pp. 7–20.
Warren, N. and Price, D. J. (1997) 'Roles of Pax-6 in murine diencephalic development', *Development*. Company of Biologists The Company of Biologists, Bidder Building, 140 Cowley …, 124(8), pp. 1573–1582.
Willis, A. M. *et al.* (2015) 'Open-loop organization of thalamic reticular nucleus and dorsal thalamus: a computational model', *Journal of neurophysiology*. American Physiological Society Bethesda, MD, 114(4), pp. 2353–2367.
Witte, H. and Bradke, F. (2008) 'The role of the cytoskeleton during neuronal polarization', *Current opinion in neurobiology*. Elsevier, 18(5), pp. 479–487.
Yogev, S. and Shen, K. (2017) 'Establishing neuronal polarity with environmental and intrinsic mechanisms', *Neuron*. Elsevier, 96(3), pp. 638–650.
Zhou, D. *et al.* (1998) 'AnkyrinG is required for clustering of voltage-gated Na channels at axon initial segments and for normal action potential firing', *The Journal of cell biology*. The Rockefeller University Press, 143(5), pp. 1295–1304.

Figures

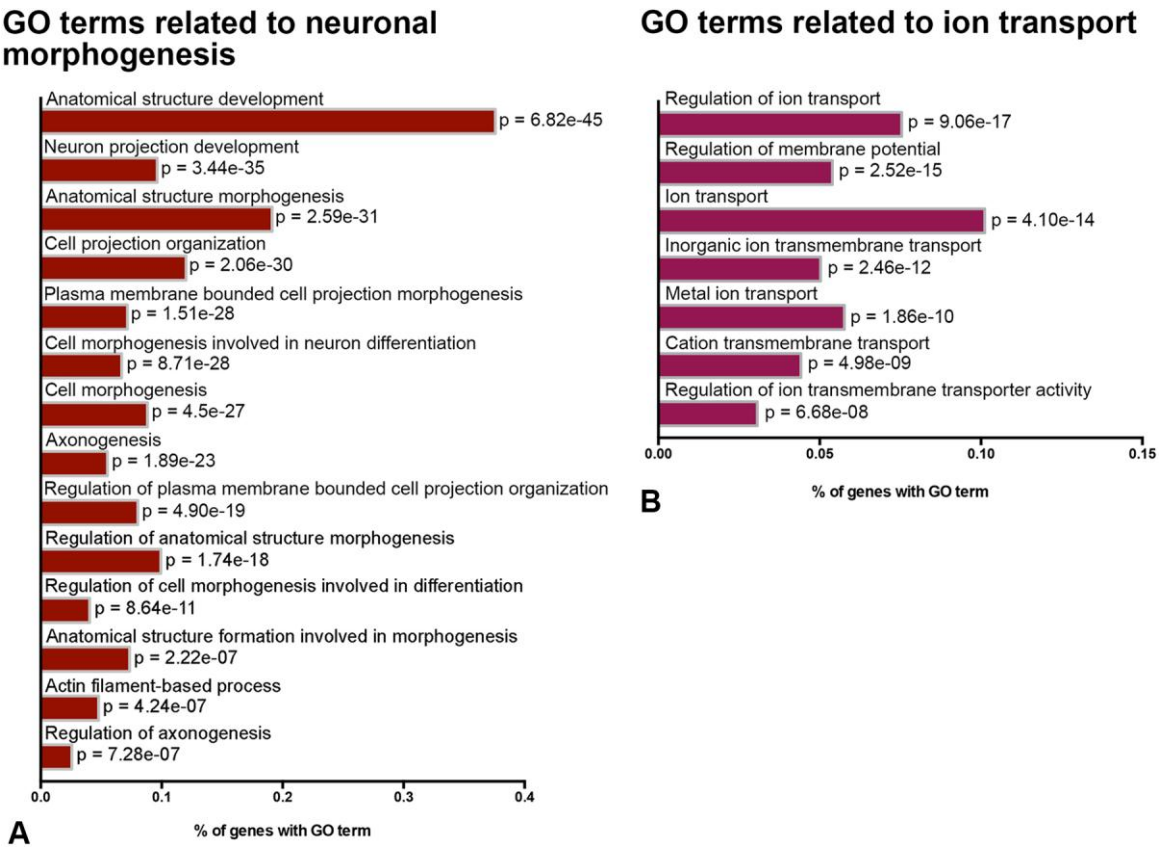

Figure 1. Pax6 deletion in the prethalamus caused upregulated expression of genes involved in neuronal morphogenesis and ion transport related GO terms. (A) The top 14 most highly enriched, non-redundant GO terms related to neuronal morphogenesis and (B) the top 7 most highly enriched, non-redundant GO terms related to ion transport in the Pax6 cKO prethalamus. See also Supplementary Table 1.

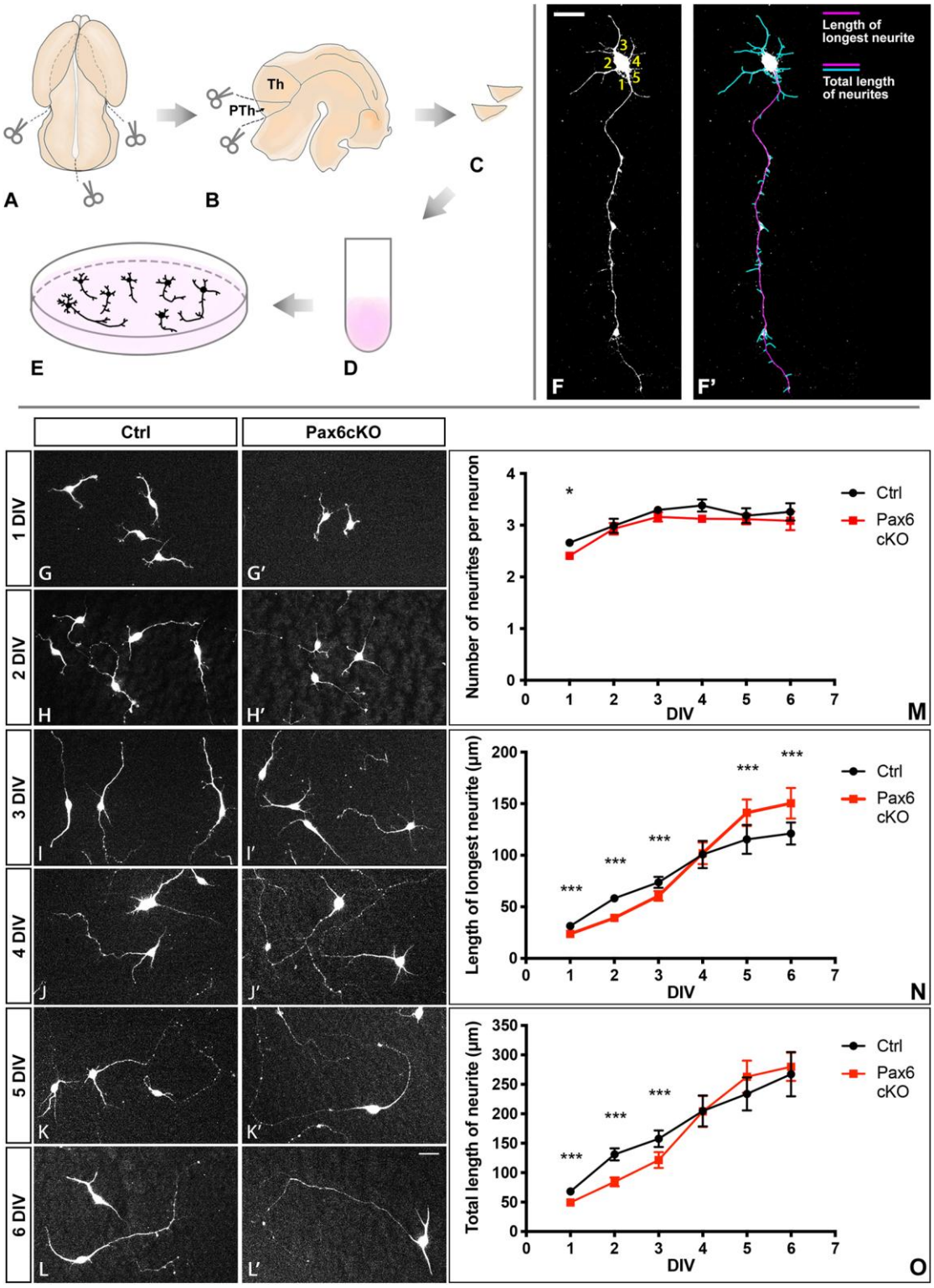

Figure 2. Neuronal morphogenesis of prethalamic neurons in vitro.

(A-E) Schematic summary of E13.5 prethalamus dissection for dissociated cell culture.

(F-F') Example of how the number of neurites (F), the length of the longest neurite and the total length of neurites (F') were measured for each neuron. Scale bar: 20µm

(G-L') Example of prethalamic neuron morphology labelled with Tuj1 from both genotypes on each DIV. Scale bar: 10µm.

(M-O) Quantification of the number of neurites (M), length of longest neurite (N) and total length of neurites (O) in Ctrl and Pax6cKO prethalamic neurons cultured 1-6DIV. Mixed-effect model, at least 100 neurons from each genotype were collected from each of 3 litters on each of the six DIVs. ***: $p<0.001$, **: $0.001<p<0.01$, *: $0.01<p<0.05$. Mean with standard error of mean (SEM).

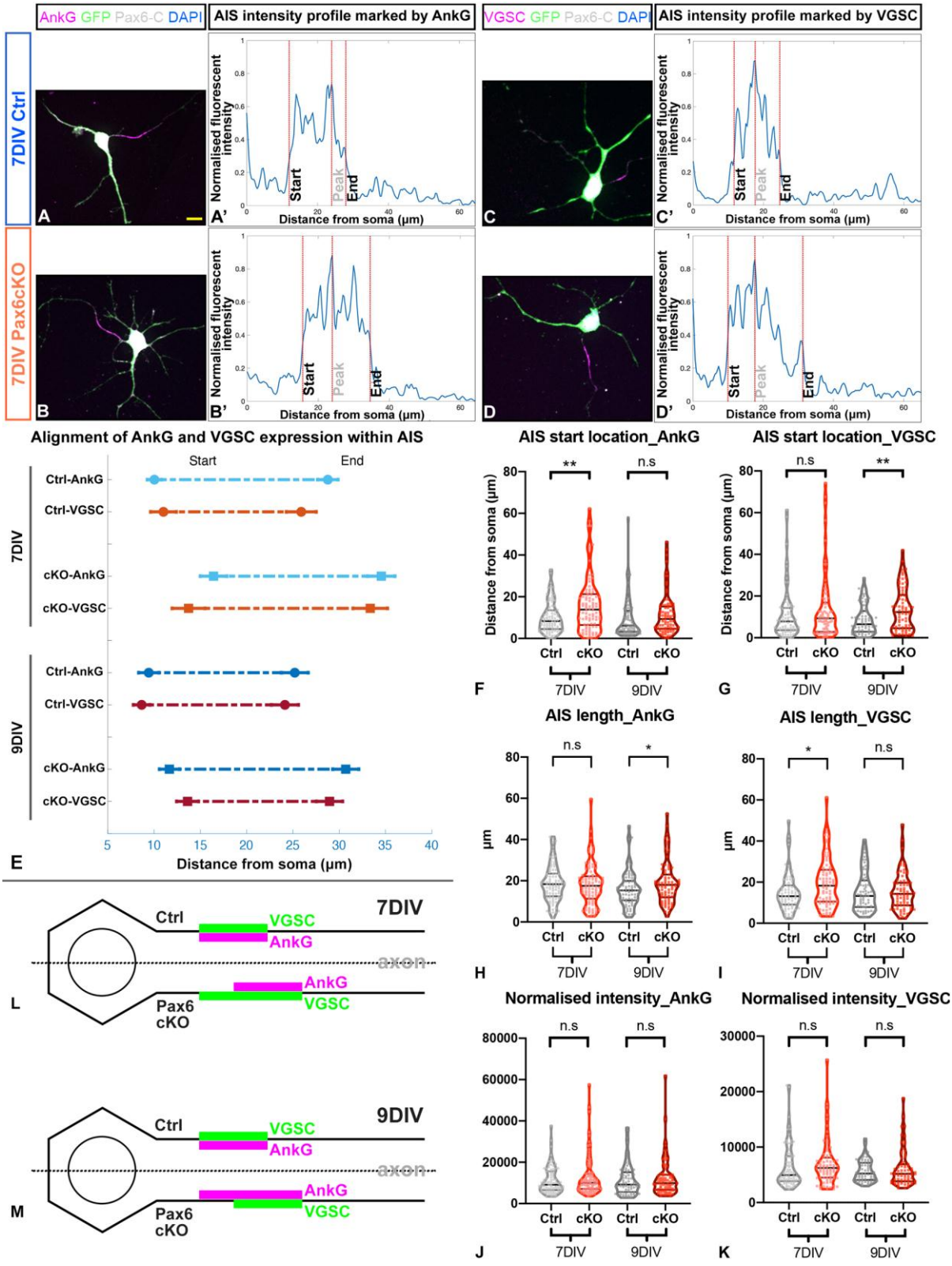

Figure 3. Loss of Pax6 changed the length and location of the AIS in the prethalamic neurons.
(A-D) Examples of immunohistochemistry staining showing localised distribution of AnkG or VGSC, marking the AIS, in prethalamic neurons cultured for 7 DIV. Scale bar: 10μm.

(A’-D’) Examples of normalised fluorescence intensity of AnkG or VGSC along the axon, termed AIS intensity profile. The peak is where the normalised fluorescence intensity is highest. The start location (close to the soma) and the end location are where normalised fluorescence intensities fall to 33% of peak (Grubb and Burrone, 2010).

(E) Alignment of the AIS length and location marked by the two markers (AnkG and VGSC) in Ctrl and Pax6cKO prethalamic neurons cultured for 7 and 9 DIV.

Comparison of the start location (F-G), length (H-I) and normalised intensity (J-K) of the AIS marked by either AnkG or VGSCs in Ctrl and Pax6cKO prethalamic neurons cultured for 7 and 9 DIV. AIS length is the distance between the start and the end location.

(L-M) Schematic summary of changes of AIS length and location in Pax6cKO prethalamic neurons at 7 and 9 DIV.

Mixed-effect model, at least 30 neurons from each genotype were collected from each litter on either 7 or 9 DIV. Three litters in total (n=3). ***: $p<0.001$, **: $0.001<p<0.01$, *: $0.01<p<0.05$. (E) Mean with SEM. (F-K) Median with interquartile range.

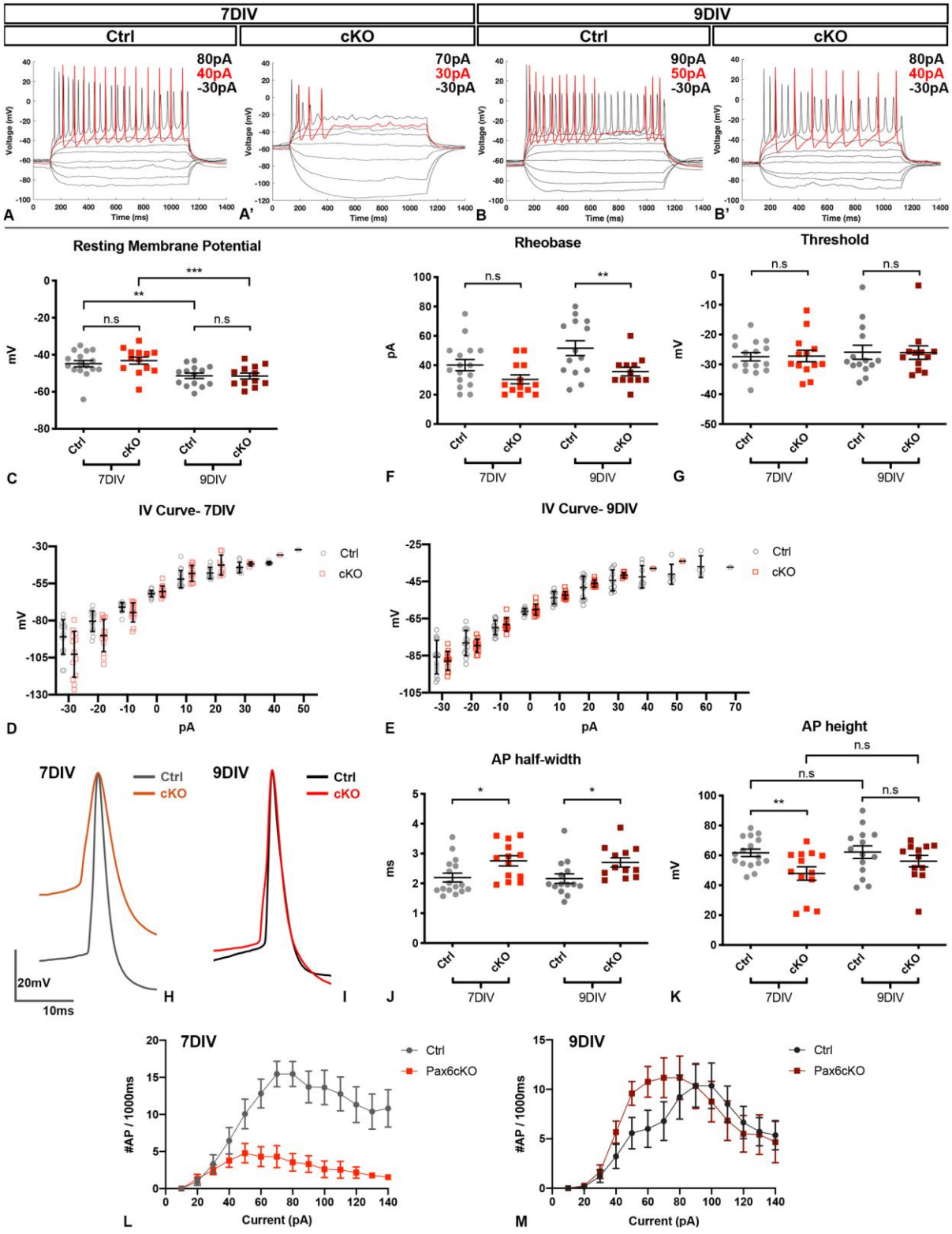

Figure 4. Pax6cKO prethalamic neurons fire APs differently at 7 and 9 DIV.

(A-B') Example of membrane potential changes of Ctrl and Pax6cKO prethalamic neurons responding to depolarising current steps (-30pA to 140pA, 10pA increments, 1000ms). Red traces: membrane potential traces at rheobases.

(C, F, G) Comparison of resting membrane potential, rheobase and threshold potential in Ctrl and Pax6cKO prethalamic neurons cultured for 7 and 9 DIV.
(D-E) IV curves in Ctrl and Pax6cKO prethalamic neurons cultured for 7 and 9 DIV.
(H-I) Aligned and overlayed traces of the first APs fired at rheobases by the Ctrl and Pax6cKO prethalamic neurons cultured for 7 and 9 DIV.
(J-K) Comparison of the half-width and height of the first AP at rheobases in Ctrl and Pax6cKO prethalamic neurons cultured for 7 and 9 DIV.
(L-M) Current frequency plot for Ctrl and Pax6cKO prethalamic neurons cultured for 7 and 9DIV, indicating differences in AP firing frequency in response to applied current steps.
Mixed effect model, 16 neurons from Ctrl 7DIV, 13 neurons from Pax6cKO 7DIV, 14 neurons from Ctrl 9DIV, 12 neurons from Pax6cKO 9DIV. 4 litters for each genotype at both DIVs (n=4). ***: $p<0.001$, **: $0.001<p<0.01$, *: $0.01<p<0.05$. (C-G, J-K) Mean with SEM. (D-E) Mean with SD.

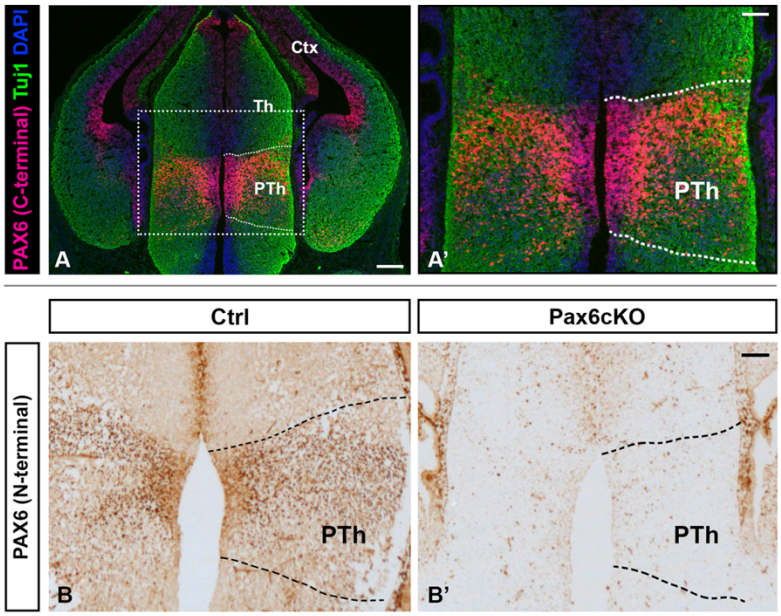

Supplementray figure 1

Fig. S1. (A-A') Immunohistochemistry showing Pax6 expression overlapping with Tuj1, a marker for postmitotic neurons, in the E13.5 prethalamus of the control littermate. PTh, prethalamus, Th, thalamus, Ctx, cortex. (B-B') Pax6 immunohistochemistry at E13.5 showing CAG^{CreER}-induced loss of Pax6 in the prethalamus following tamoxifen administration at E9.5. (C) The top 14 most highly enriched, non-redundant GO terms related to neuronal morphogenesis and (D) the top 7 most highly enriched, non-redundant GO terms related to ion transport in the Pax6 cKO prethalamus. Scale bar: (A) 250 μm; (A', B-B') 100μm. See also Supplementary Table 1.

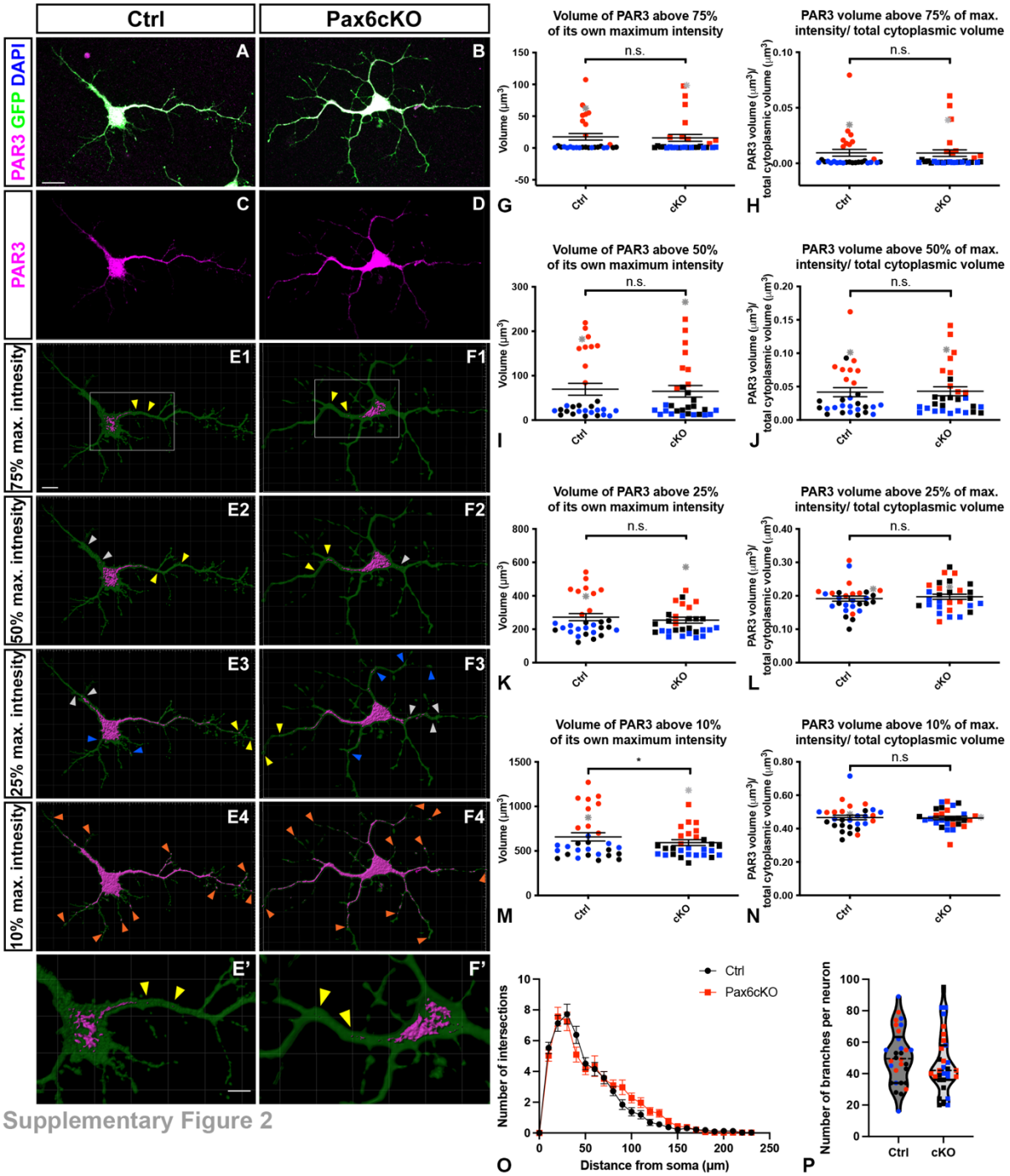

Supplementary Figure 2

Fig. S2. Distribution of Par3 proteins and neurite branching of the developing prethalamic neurons at 3DIV. (A, B) Prethalamic neurons from the Ctrl (A) and Pax6cKO (B) embryos were cultured for 3DIV and stained for Par3, GFP and DAPI. **(C, D)** Par3 expression within the cytoplasm of the neurons. **(E1-F1)** Par3 expression within the cytoplasm when the intensity threshold was set at 75% of the maximum intensity of the Par3 channel. The majority of the Par3 volumes were distributed within the soma. However, Par3 volumes were also found in the stem of the longest neurites (yellow arrowheads). **(E2-F2)** Par3 expression within the cytoplasm when the intensity threshold was set at 50% of the maximum intensity of the Par3 channel.

More Par3 volumes were detected in the soma, the stem of the longest neurites (yellow arrowheads), as well as in other neurites (grey arrowheads). **(E3-F3)** Par3 expression within the cytoplasm when the intensity threshold was set at 25% of the maximum intensity of the Par3 channel. Par3 volumes within the cytoplasm continued to increase. Par3 volumes could be found at the tip of the longest neurites (yellow arrowheads) and other neurites (grey and blue arrowheads). **(E4-F4)** Par3 expression within the cytoplasm when the intensity threshold was set at 10% of the maximum intensity of the Par3 channel. PAR3 volumes had filled up the cytoplasm and could be found at almost all the tip of the neurites and protrusions (orange arrowheads). **(E'-F')** Zoom in on the boxed area in E1 and F1. Scale bars: A-D, 15μm, E1-F5, 10μm, E'-F', 5μm. **(G-N)** Comparison of Par3 volumes and percentage of Par3 volumes against the cytoplasmic volume between the Ctrl and the Pax6cKO prethalamic neurons. Each dot (data point) represented the value of Par3 volume (G, I, K, M) or Par3 volume/ total cytoplasmic volume (H, J, L, N) from each neuron at a specific threshold. Data derived from the corresponding images in panels A-F are shown as grey asterisks in panels G-N. 10 neurons with the Ctrl and Pax6cKO genotypes from each of 3 cultures from separate litters were measured. Mixed-effect model. Mean ± SEM. *: $p<0.05$. The data points of the neurons from the same litter were marked with the same colour. **(O)** Sholl analysis showed no significant difference in the number of neurite intersections between 10 and 240 μm from the soma between the Pax6cKO and the control prethalamic neurons, $p=0.194$. **(P)** Evaluation of number of branches per neuron showed no significant difference between the Pax6cKO and the control prethalamic neurons, $p=0.238$. 10 neurons with the Ctrl and Pax6cKO genotypes from each of 3 cultures from separate litters were measured. Mixed-effect model. Mean ± SEM.

Table S1. List of significantly up- and downregulated (adjusted p<0.05) genes and GO terms in the E13.5 prethalamus after induced acute Pax6 deletion at E9.5. Related to Figure 1.

Genes	LFC	P value	Description
GEFs for Rac			
Dock4	1.03	3.39E-10	dedicator of cytokinesis 4
Dock2	0.86	0.00196	dedicator of cytokinesis 2
Dock3	0.68	0.00300	dedicator of cytokinesis 3
Dock9	0.66	0.00671	dedicator of cytokinesis 9
Dock10	0.76	0.00339	dedicator of cytokinesis 10
Dock8	0.95	0.00178	dedicator of cytokinesis 8
Scaffold for GEFs			
Elmo1	0.87	2.21E-10	engulfment and cell motility 1
Scaffold for CDC42			
Fgd1	0.57	0.00362	FYVE, RhoGEF and PH domain containing 1
Fgd5	1.04	3.11E-05	FYVE, RhoGEF and PH domain containing 5
Fgd2	0.67	0.00234	FYVE, RhoGEF and PH domain containing 2
Fgd6	0.65	0.00503	FYVE, RhoGEF and PH domain containing 6
GAP for Rho and Rac			
Srgap3	0.92	0.00086	SLIT-ROBO Rho GTPase activating protein 3
Rac			
Rnd1	0.77	2.55E-07	Rho family GTPase 1
Actin-bundling			
Ablim1	0.59	0.00253	actin-binding LIM protein 1
Ablim3	1.19	7.20E-07	actin binding LIM protein family, member 3
Ablim2	0.91	0.00342	actin-binding LIM protein 2
Strip2	1.80	4.32E-07	striatin interacting protein 2
Anti-capping for actin			
Enah	0.67	0.00391	enabled homolog (Drosophila)
Membrane curvature			
Pacsin1	0.81	0.00546	protein kinase C and casein kinase substrate in neurons 1
Microtubule polymerisation/bundling			
Mapt	1.16	4.90E-08	microtubule-associated protein tau
Map6	0.70	0.00732	microtubule-associated protein 6
Map9	0.60	0.00746	microtubule-associated protein 9
Map2	0.32	0.01108	microtubule-associated protein 2
Mark1	0.78	0.00014	MAP/microtubule affinity-regulating kinase 1
Mark4	0.76	0.00720	MAP/microtubule affinity-regulating kinase 4
Apc2	0.86	0.00485	adenomatosis polyposis coli 2
Apc	0.78	0.00820	adenomatosis polyposis coli

Crmp1	0.32	0.00312	collapsin response mediator protein 1
Dpysl5	0.66	0.00500	dihydropyrimidinase-like 5
Par3/6 complex component			
Prkcz	0.37	0.00431	protein kinase C, zeta
Kif3a	0.45	0.00484	kinesin family member 3A
Tiam1	0.66	0.00821	T cell lymphoma invasion and metastasis 1
Arhgap35	0.59	0.01060	Rho GTPase activating protein 35
Smurf1	0.53	0.00328	SMAD specific E3 ubiquitin protein ligase 1
Pard3b	0.80	0.00822	par-3 family cell polarity regulator beta
Apc	0.78	0.00820	adenomatosis polyposis coli
Cytoskeleton protein in the axon initial segment			
Ank3	1.19	0.00105	ankyrin 3, epithelial
Sptb	1.17	0.00054	spectrin beta, erythrocytic
Sptbn1	1.03	0.00096	spectrin beta, non-erythrocytic 1
Sptbn4	1.36	4.52E-06	spectrin beta, non-erythrocytic 4
Voltage-gated Sodium channels (VGSCs)			
Scn1a	0.77	0.00123	sodium channel, voltage-gated, type I, alpha
Scn3b	0.72	2.96E-06	sodium channel, voltage-gated, type III, beta
Scn2b	0.58	0.00118	sodium channel, voltage-gated, type II, beta
Scn3a	0.39	0.00502	sodium channel, voltage-gated, type III, alpha
Rapidly inactivating A-type K+ channel			
Kcna4	1.87	1.40E-16	potassium voltage-gated channel, shaker-related subfamily, member 4
Kcnc3	1.02	0.00040	potassium voltage gated channel, Shaw-related subfamily, member 3
Kcnc4	0.79	0.00252	potassium voltage gated channel, Shaw-related subfamily, member 4
Kcnd1	0.61	0.00769	potassium voltage-gated channel, Shal-related family, member 1
Kcnd3	1.02	3.78E-10	potassium voltage-gated channel, Shal-related family, member 3
Kcnd2	0.84	9.81E-07	potassium voltage-gated channel, Shal-related family, member 2
Voltage-gated Ca2+ channels			
Cacna1e	1.09	0.00012	calcium channel, voltage-dependent, R type, alpha 1E subunit
Cacna2d2	0.68	0.00930	calcium channel, voltage-dependent, alpha 2/delta subunit 2
Cacna1a	0.61	0.00114	calcium channel, voltage-dependent, P/Q type, alpha 1A subunit
Cacna2d4	1.87	2.98E-08	calcium channel, voltage-dependent, alpha 2/delta subunit 4
Cacna1g	1.21	4.11E-07	calcium channel, voltage-dependent, T type, alpha 1G subunit
Hyperpolarization-activated cyclic nucleotide–gated (HCN) channels			
Hcn2	0.95	1.12E-05	hyperpolarization-activated, cyclic nucleotide-gated K+ 2
Hcn4	0.70	0.00481	hyperpolarization-activated, cyclic nucleotide-gated K+ 4
Hcn3	0.40	0.00852	hyperpolarization-activated, cyclic nucleotide-gated K+ 3

Table S2. List of genes found in the neuronal morphogenesis and ion transport GO terms that encode proteins with specific neuronal functions. LFC, log-fold change.

Click here to download Table S2